

Tailoring the γ - γ' - γ'' Dual Superlattice Microstructure of INCONEL[®] 725 by High Temperature Aging and Nb/Ta Additions for Superior Creep Properties



Stoichko Antonov, Chang-Yu Hung, Jeffrey A. Hawk, Paul D. Jablonski, and Martin Detrois

Abstract Next-generation energy systems require superior resistance to creep deformation due to the considerably prolonged exposure times at operating stress and temperature. To improve the elevated temperature properties of INCONEL[®] 725 (IN725), a corrosion-resistant alloy, several variants with different Ti/Al ratios and judicious amounts of Nb and Ta were made. Furthermore, a high temperature aging (HTA) heat treatment, designed to promote favorable precipitate phase formation, was explored. These adjustments allowed to tailor the amount and type of precipitate strengthening which led to significant increases in time to failure. The Ti/Al ratio was used to favor the formation of γ' or γ'' precipitates. Compact morphology precipitates, consisting of γ' precipitates surrounded by a γ'' shell, were formed in alloys with a low Ti/Al ratio. The HTA increased the creep life of various alloy formulations up to a maximum improvement of 371% as compared to the standard aging heat treatment. The Nb and Ta additions had a similar effect on increasing creep life by promoting and stabilizing γ'' precipitation. The positive effect of the additions was even more pronounced when coupled with the HTA. A phase stability study with up to 10,000 h exposure at 700 °C revealed that the compact morphology helped in slightly reducing coarsening of the γ' precipitates, although the effect on creep was not significant. The findings of this study enable design of dual superlattice alloys through microstructural engineering that yields superior performance and can be applied to a wide range of alloys in the IN718 and derivatives family.

Keywords Ni-based superalloy · Inconel 725 · Creep · Phase stability · Dual superlattice

S. Antonov (✉) · C.-Y. Hung · J. A. Hawk · P. D. Jablonski · M. Detrois
National Energy Technology Laboratory, 1450 Queen Ave. SW, Albany, OR 97321, USA
e-mail: Stoichko.Antonov@netl.doe.gov

C.-Y. Hung
NETL Support Contractor, 1450 Queen Ave. SW, Albany, OR 97321, USA

© The Minerals, Metals & Materials Society 2023
E. A. Ott et al. (eds.), *Proceedings of the 10th International Symposium on Superalloy 718 and Derivatives*, The Minerals, Metals & Materials Series,
https://doi.org/10.1007/978-3-031-27447-3_10

Introduction

INCONEL[®] 725, i.e. IN725, is a derivative of INCONEL[®] 625 through the addition of Ti with aim of promoting the formation of γ' precipitates [1]. This precipitation strengthened Ni-based superalloy has high strength and good corrosion resistance [2], making it a material of choice for a wide variety of intermediate-temperature applications, especially considering that it does not contain costly Co additions. Interestingly, although IN625 was designed to be a solid-solution strengthened alloy, subsequent investigations have conclusively shown the precipitation of the γ'' phase at temperatures <750 °C. As a result, the typical microstructure of IN725 also consists of a face-centered cubic (FCC) matrix with embedded γ'' precipitates, however, the Ti addition also promotes the formation of γ' precipitates; the fraction of the two secondary phases can vary depending on the employed heat treatment [3]. The γ' precipitates are $\text{Ni}_3(\text{Al}, \text{Ti})$ with ordered FCC $L1_2$ crystal structure, while the γ'' phase is typically Ni_3Nb and has an ordered tetragonal $D0_{22}$ crystal structure. Both precipitates have solubility for elements such as Co, Cr, Nb, and Mo among others. Generally, the γ' phase is preferred for high temperature applications of Ni-based alloys due to its higher solvus temperature and superior stability compared to that of the γ'' precipitates. However, the latter offers more potent strengthening due to the high coherency stresses with the matrix, that can significantly extend the creep life in temperature regimes where the γ'' precipitates are stable. Of note, when co-precipitated in a compact morphology, as reported by Cozar et al. [4, 5], the γ'' shell is thought to be beneficial in preventing significant coarsening of the γ' precipitates and further improve the mechanical properties of the alloy.

In addition to the γ' and γ'' phases, IN725 also contains carbides such as MC (Ti/Nb rich), $M_{23}C_6$ (primarily Cr-rich), and M_6C (Mo-rich) which are located along the grain boundaries (GBs) [3]. Furthermore, η phase has been reported to form at temperatures between 750 and 900 °C for times ranging from 10 to 100 h [6]. The η phase has an ordered hexagonal $D0_{24}$ crystal structure and a composition consisting of Ni_3Ti . Similar to δ phase precipitates, which have a $D0_a$ crystal structure and a composition of Ni_3Nb , the effect of η phase on the mechanical properties of Ni-based superalloys has been the subject of numerous investigations. Small and stable precipitates have been shown to be beneficial to alloy 718Plus by slowing down fatigue crack growth rates [7], while unstable precipitates were found to be detrimental to the creep performance of alloy 263 [8]. Small δ platelets are formed in IN718 using a high temperature aging heat treatment [9]. Finally, η - Ni_6AlNb and the coexistence of δ and η phases have been reported in several alloys [10, 11].

Using IN725 in high-temperature applications would be very valuable to fully utilize its superior corrosion resistance and relatively low cost. Particularly, alloys capable of operating for extended times at temperature in demanding environments are needed for next-generation land-based energy systems [12]. However, to date, there have been very few high-temperature mechanical properties reported for IN725, with most assessments being up to 550 °C or 650 °C [13, 14]. This investigation explores the high-temperature creep properties of several variants of IN725 that

were designed with several key parameters. The stability of the γ' and γ'' phases was explored using changes from the nominal composition of IN725 according to the Ti/Al ratio. Additions of Ta and Nb were chosen to promote the formation of desirable phases and a high temperature aging heat treatment was designed to increase the precipitation of those features. Compared to the baseline alloy tested at 700 °C/483 MPa, condition most representative of IN725, the creep life of the variants increased by up to 256%. The relationships between alloying, microstructural formation and evolution, and creep properties are presented and discussed.

Methods

The alloys were developed starting from the composition of commercial IN725, as described in Ref. [2]. A computational approach was utilized to obtain the targeted compositions using Thermo-Calc with the TCNi8 database for phase formation and JMatPro for kinetics. The baseline alloy, referred to as STD, consists of near-nominal composition for IN725 with a Ti/Al ratio of 4.3 (calculated using at.% throughout this study). A slightly higher Ta-containing version was made and named A. Then, the Ti/Al ratio was systematically decreased from variants A to D with values equal to 5.4, 1.3, 1.1, 0.7 in alloys A, B, C, and D, respectively. Finally, the amount of Nb + Ta was increased to 2.7 at.% in variants with the high and low Ti/Al ratio, namely STD and D, to promote the formation of GB phases, such as δ phase precipitates, according to plots from Ref. [11] or γ'' precipitates within the matrix. Tantalum was added to alloys STD and D to form alloys E1 and E, respectively. Similarly, Nb was added to alloys STD and D to form alloys F2 and F, respectively.

High-purity, industry grade, stock materials were used to constitute the compositions of the alloys and form 8 kg cylindrical ingots measuring 75 mm in diameter using vacuum induction melting (VIM). The charges were melted to a 50 °C superheat temperature under 200 Torr Ar partial pressure. Following solidification, ~5 mm thick slices were cut from the top of each ingot for chemistry analysis. Major elements were determined using X-ray fluorescence (XRF) on a Rigaku ZSX Primus II while C was determined using combustion analysis on LECO systems. The ingots were homogenized in a vacuum heat treatment furnace under 50 Torr Ar partial pressure and using Ar forced gas fan cooling. The heat treatment schedule was optimized computationally for the alloys based on their chemistry and the ingot microstructure to reduce the predicted residual elemental inhomogeneity to below 1% [15]. The heat treatment cycle consisted of 1030 °C for 1 h, 1065 °C for 3 h, 1090 °C for 3 h, 1115 °C for 3 h, 1135 °C for 6 h, and 1150 °C for 72 h. Hot working consisted of steps of forging followed by steps of hot rolling with reheat between each pass to produce plates measuring 10 mm in thickness with an equiaxed grain structure. The last reheat step was used as a solution heat treatment.

Two separate aging heat treatments were investigated. The first consists of the standard aging heat treatment for IN725 and is referred to as standard aging (SA): 730 °C for 8 h followed by cooling to 620 °C at 1 °C/min and holding at 620 °C for

8 h. The alternate aging heat treatment was designed to promote the formation of precipitate phases at higher temperatures, and thereby, is referred to as high temperature aging (HTA), described as follows: 800 °C for 20 h followed by cooling to 750 °C at 1 °C/min and holding at 750 °C for 8 h. The aging heat treatments were performed in the vacuum heat treatment furnace under 50 Torr Ar partial pressure and Ar forced gas fan cooling was performed at the end of the cycles. Specimens characterized and mechanically tested received either the SA or HTA heat treatments.

Cylindrical creep test specimens were produced with 76 mm in overall length, 10 mm in overall diameter with ANSI 3/8 × 16 threaded ends, and a reduced gage area. The reduced gage section measured 32 mm in length and 6.3 mm in diameter. Creep screening was performed according to ASTM E139 standard using a dead weight creep frame [16]. Four conditions were selected for constant load creep testing: 700 °C/483 MPa, 727 °C/414 MPa, 750 °C/345 MPa, and 790 °C/207 MPa. Not every alloy was tested at each condition, but all alloys were tested at 700 °C/483 MPa.

After standard metallographic sample preparation, observation of the microstructures was performed on a FEI Inspect F scanning electron microscope (SEM) in backscatter electron mode and equipped with an Oxford Instrument X-Max energy dispersive spectrometer (EDS) for phase characterization. Transmission electron microscopy (TEM) samples were prepared by extracting Ø3 mm discs from as-aged material and from the grip sections of post-creep specimens. Following grinding on progressive grit papers to ~70 µm, the TEM blanks were thinned to electron transparency using twin-jet polishing in a solution of 20% perchloric acid and 80% ethanol at -16 °C and 18 V. A JEOL JEM 2100PLUS, operating at 200 kV, was used for selected area diffraction (SAD) and bright field (BF), dark-field (DF) and high resolution (HR) imaging.

Results

Alloy Chemistry

The measured chemistries of the alloys are listed in Table 1. The high Ti/Al ratio alloys are STD, E1, F2, and A. Note: the Ti/Al ratio was lower in alloy STD likely due to minor Al loss in the other alloys which occurred during melting. In this series, the Ta content was increased to 3.6 wt.% in E1 and the Nb content was raised to 4.6 at.% in F with a sum Nb + Ta between 2.4 and 2.7 at.%. The Ti/Al ratio was decreased from A to D with values equal to 5.4, 1.3, 1.1, and 0.7 in A, B, C, and D, respectively. Finally, the low Ti/Al ratio series included alloy D and high-Ta variant E with 3.5 wt.% Ta and high-Nb variant F with 4.5 wt.% Nb. The sum of Nb + Ta is between 2.5 and 2.8 at.% for both alloys. Thus, this alloy series allows for the investigation of the effect of the Ti/Al ratio and additions of Nb or Ta to alloys with the highest and lowest Ti/Al ratios.

Table 1 Composition of the alloys with Ni balanced from XRF analysis (major elements), combustion analysis (C), and addition to the melt (B) in wt.% except for the ratio Ti/Al and sum Nb + Ta in at.%

Alloy	Cr	Mo	Ti	Al	Nb	Ta	Fe	Mn	Si	C	B	Ti/Al	Nb + Ta
<i>High Ti/Al Ratio</i>													
STD	21.2	7.1	1.82	0.24	3.4	0.2	3.9	0.04	0.02	0.039	0.003	4.3	1.8
E1	20.5	7.0	1.87	0.20	3.4	3.6	3.8	0.05	<0.01	0.049	0.003	5.4	2.7
F2	20.6	7.1	1.88	0.19	4.6	0.4	3.9	0.05	<0.01	0.049	0.003	5.6	2.4
<i>Varying Ti/Al Ratio</i>													
A	21.2	7.1	1.84	0.19	3.4	0.4	3.9	0.05	0.01	0.040	0.003	5.4	1.8
B	21.2	7.1	1.41	0.60	3.4	0.4	3.9	0.04	0.02	0.039	0.003	1.3	1.9
C	21.2	7.1	1.30	0.68	3.4	0.4	3.9	0.05	0.01	0.040	0.003	1.1	1.9
<i>Low Ti/Al Ratio</i>													
D	21.2	7.1	1.10	0.85	3.4	0.4	3.9	0.06	0.03	0.044	0.003	0.7	1.9
E	21.2	7.0	1.15	0.89	3.4	3.5	3.9	0.04	0.02	0.038	0.003	0.7	2.8
F	21.3	7.1	1.13	0.84	4.5	0.4	3.9	0.04	0.01	0.040	0.003	0.8	2.5

Microstructure

Analysis of the microstructure of the alloys following hot working and solution heat treatment revealed equiaxed grain structures with similar grain sizes ranging from 42 to 47 μm . The grain size was calculated using the linear intersect technique [17] with four regions considered, each used to perform four measurements. For each alloy, half of the material received the SA aging heat treatment while the other half received the HTA heat treatment. The microstructures observed using the SEM and including GB regions are shown in Fig. 1. First, the microstructures following SA (commercial heat treatment for IN725) revealed very fine precipitates that could hardly be resolved with the SEM, as shown in the insets of Fig. 1. The GBs of alloy F, however, contained larger precipitates when compared to alloys STD, D, and E. Images for E1 and F2 are not available at the time of writing.

The microstructures of the alloys following the HTA heat treatment revealed coarser precipitates. Particularly, a dense distribution of γ' and/or γ'' particles can be resolved within the grain interior. Typically, the γ' phase appears darker in Z-contrast backscatter images due to the higher content of light-element Al, while γ'' appears bright from the Nb and other heavy refractory elements. Various GB phases also formed. Dark, blocky precipitates were found in all alloys, and EDS analysis performed on similar but overaged specimens (to enable coarsening and more accurate EDS measurements) associated them with Cr-rich M_{23}C_6 carbides. The small, blocky, and bright precipitates are likely M_6C due to high Mo concentrations and traces of Si [18]. This correlates well with other investigations of IN725

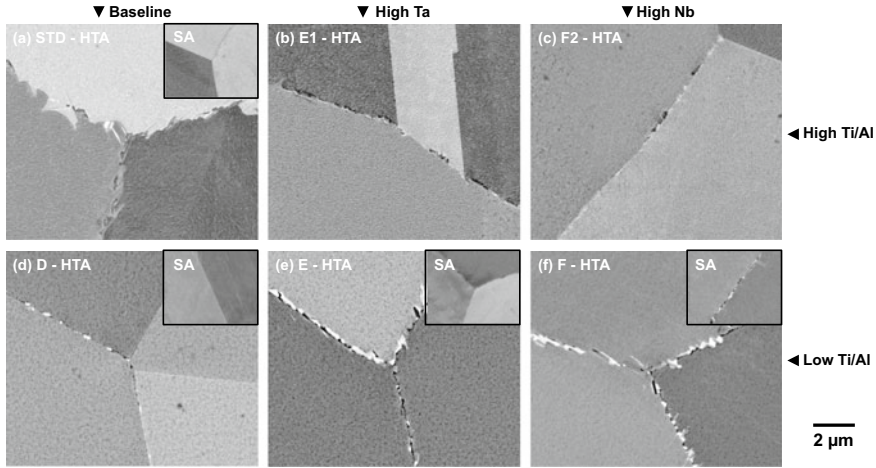


Fig. 1 SEM images of the microstructure of alloy **a** STD, **b** E1, **c** F2, **d** D, **e** E and **f** F including grain boundaries following the HTA heat treatment with insets for the SA heat treatment condition for alloys STD, D, E, and F

[3]. Overall, no significant differences are noticeable between the alloys, particularly STD, Fig. 1a, E1, b, F2, c and D, d. Alloys E, Fig. 1e and F, 1f, however, contained discrete needle/rod-shaped precipitates consistent with δ or η phase and a primarily $\text{Ni}_3(\text{Nb}, \text{Ti})$ composition. Such precipitates were also found in STD and F2 to a lesser extent. Additional details on the EDS analysis can be found in Ref. [19].

Higher resolution images of the γ/γ' and/or γ'' were taken using TEM and the results for alloys STD, D, E, and F heat treated using either the SA or HTA are shown in Fig. 2. In general, the microstructural components and morphology of each alloy are the same between the two heat treatments, however, the size is much coarser following HTA. The STD alloy formed mostly $\gamma''/\gamma'/\gamma''$ sandwich-type structures, where the γ'' formed on only two faces of the γ' precipitates. Alloy D predominantly formed γ' precipitates. To better show the absence or presence of γ'' in this alloy, DF images using the shared γ'/γ'' (100) reflections are shown in Fig. 2b and f. Interestingly, a small fraction of γ'' precipitates were observed for the SA condition, while γ'' was not observed at all post-HTA. Alloys E and F show similar microstructures to each other following SA, Fig. 2c and d, respectively, and after HTA, Fig. 2g and h, respectively, where the γ'/γ'' precipitates exhibit compact morphologies in both aging conditions. The major microstructural difference between the two alloys being that alloy F has a slightly thicker and higher fraction of γ'' precipitates, and that the precipitates are significantly coarser after HTA compared to SA.

The microstructures of alloys E1 and F2 after HTA (these alloys were not subjected to the SA) were also observed by TEM and representative microstructures are shown in Fig. 3. The addition of Ta and Nb to E1 and F2, respectively, stabilized the γ'' precipitates, such that a γ/γ'' microstructure (with the absence of any γ' precipitates) formed. The two alloys exhibit similar γ/γ'' microstructure with three variants of

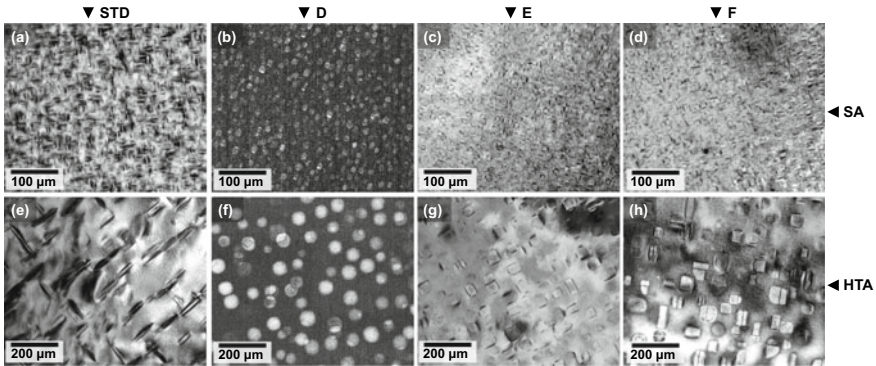


Fig. 2 TEM images of alloys **a, e** STD, **b, f** D, **c, g** E and **d, h** F for the γ' and/or γ'' precipitates following the SA (**a–d**) or HTA (**e–h**) heat treatment. *Note* Images **a, c, d, e, g,** and **h** are BF, while **b** and **f** are DF

rather coarse γ'' precipitates. Figure 3c and d shows DF images of one of the γ'' variants, obtained using the shared γ'/γ'' (100) reflection. As can be seen, γ' precipitates were not present, and the fraction of γ'' precipitates tends to be higher in alloy F, Fig. 3d. Such observations were performed at other locations and with the other shared γ'/γ'' reflections as to more conclusively determine whether γ' formed in these alloys; it did not.

To better understand the formation and distribution of the γ'' precipitates in some of the alloys, HRTEM was performed. As shown in Fig. 2b and f, a small fraction of γ'' precipitates were observed only after SA in alloy D. The diffraction patterns showed faint γ'' reflections, even when such precipitates were not observed using DF imaging. Figure 4a shows a HRTEM image of a γ' precipitate in alloy D after SA aging. Interestingly, 2–3 atomic layer thick γ'' structure was observed on the faces of the γ' precipitate, and such a structure was observed on most of the γ' precipitates in this alloy. Figure 4b shows an HRTEM image of alloy F after HTA, where the γ'/γ'' compact structure was readily apparent in Fig. 2h. Indeed, the faces of the γ' precipitates are entirely covered (edge-to-edge) with γ'' that is tens of atomic layers thick. Finally, an HRTEM image from a γ'' precipitate in alloy E1 after HTA such as the ones in Fig. 3a and c is shown in Fig. 4c. The γ'' precipitate was not connected to any other type of precipitate, and γ' structure was not observed.

Creep Properties

The results from all performed creep tests are shown in the form of a Larson-Miller parameter (LMP) plot in Fig. 5. The alloys were all tested at 700 °C and 483 MPa in either SA or HTA heat treatment condition, at the exception of alloys E1 and F2 only tested after HTA. Additional testing was performed at lower stresses for

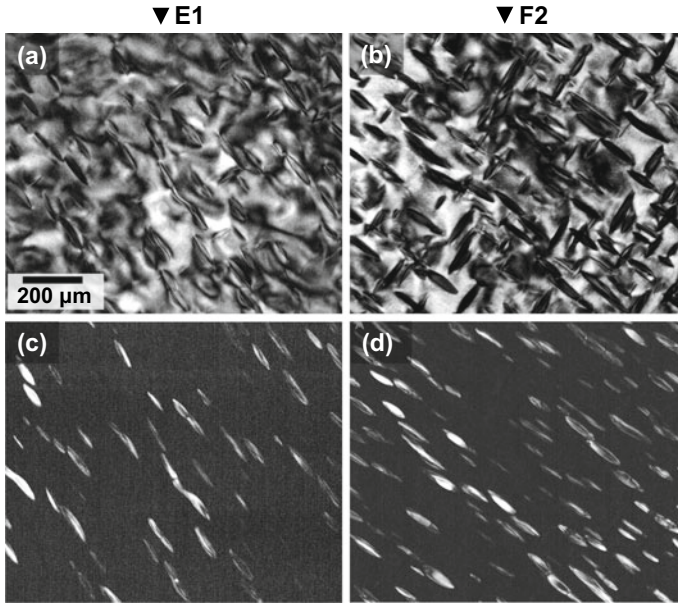


Fig. 3 TEM images of alloys **a, c** E1, and **b, d** F2, for the γ'' precipitates following HTA heat treatment, where **a, b** show BF images, and **b, d** show DF images at the same location

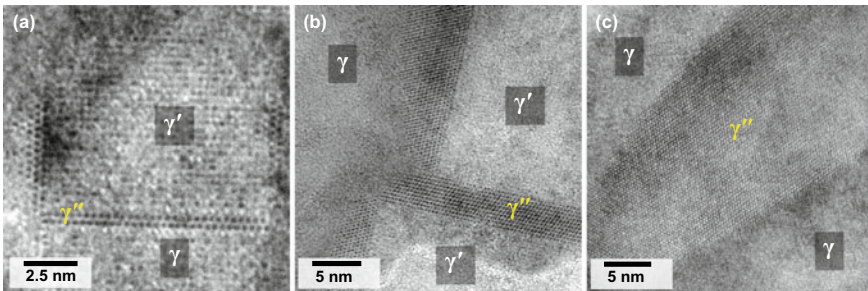
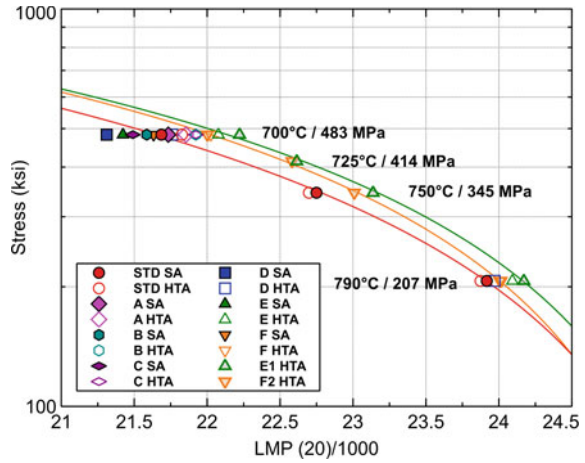


Fig. 4 HRTEM images of the $\gamma/\gamma'/\gamma''$ interfaces in alloys **a** D with the SA heat treatment, **b** F with the HTA heat treatment and **c** E1 with the HTA heat treatment

alloy STD to form a curve for the baseline creep properties. The testing temperature was raised for testing time constraints. From creep at 700 °C and 483 MPa, it is shown that the LMP decreases from 21.69 to 21.31 with decreasing Ti/Al ratio from alloy STD to D. However, using the HTA instead of the SA heat treatment increased the LMP values to above those for alloy STD with SA. The best-performing alloys were those with added Nb and Ta, namely E, F, E1 and F2, and with the HTA heat treatment. Particularly, alloy E1 HTA outperformed all other alloys on the LMP plot with additional testing performed to draw a fitting curve for comparison to alloy

Fig. 5 Larson-Miller plot for testing of the alloys under four conditions and after the SA or HTA heat treatment



STD SA and F2 HTA. The LMP increased by 0.54 at 700 °C/483 MPa and 0.25 at 790 °C/207 MPa from alloy STD SA to alloy E1 HTA.

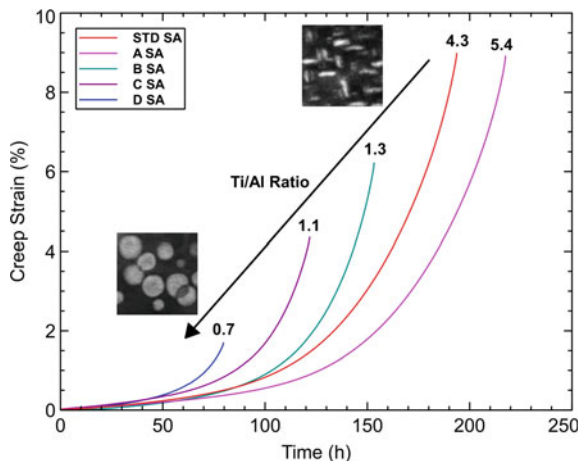
Discussion

A series of alloys based on IN725 was designed with several aspects that led to improvements in creep performance [20, 21]. The Ti/Al ratio was varied, additions of Nb and/or Ta were considered, and a high temperature aging (HTA) heat treatment was compared to the standard aging (SA) for IN725. From Fig. 5, the HTA combined with Nb or Ta additions led to the best properties. The effect of each design attribute is described in the following sections.

Effect of the Ti/Al Ratio

The Ti/Al ratio was decreased from alloys STD/A to D which led to changes in the microstructural features of each variant. Minimal differences were found along the GBs when comparing high Ti/Al ratio alloy STD and low Ti/Al ratio alloy D following the HTA heat treatment, Fig. 1a and d, respectively. More of the elongated δ/η platelets were found in alloy STD. A more significant microstructural difference was observed within the grains. As shown in Figs. 2 and 3, the high Ti/Al ratio alloys STD, E1, and F2 primarily contained γ'' precipitates while the low Ti/Al ratio alloys D, E, and F mostly contained γ' precipitates surrounded by a varying fraction of γ'' precipitates. Only alloy D after HTA contained just γ' precipitates. The decrease in the Ti/Al ratio consisted of a ~40% decrease in the Ti content and a ~4.5× increase

Fig. 6 Creep strain as a function of time for testing at 700 °C and 483 MPa for the alloys with decreasing Ti/Al ratio and following the SA heat treatment. TEM images of the precipitates in alloy STD and D in the aged condition are provided



in the Al content. Therefore, the decrease in the Ti/Al ratio stabilized the γ' -Ni₃Al precipitates over the γ'' -Ni₃Nb particles.

The creep curves from testing of the alloys in the SA condition at 700 °C and 483 MPa are shown in Fig. 6 with the alloy Ti/Al ratio denoted for each curve. The decrease in Ti/Al ratio correlated well with a decrease in creep life and ductility. Thus, a 63% decrease in creep life and 81% decrease in elongation to failure were measured from alloys A to D. Testing of the alloys in the HTA condition revealed a similar trend with respect to creep ductility, as highlighted in Fig. 7 which shows the elongation to failure as a function of time to failure. However, the creep lives of B HTA and C HTA were greater than those for STD HTA, A HTA, and D HTA. Therefore, the switch from predominant γ'' to γ' precipitate strengthening was associated with a loss in creep ductility and creep life, the latter being more evident for the SA heat treatment. The γ'' phase is known to provide more potent strengthening due to the high coherency stresses with the γ matrix. The effect of the HTA heat treatment is further discussed in the next section.

Effect of the Aging Temperature

The HTA heat treatment had a pronounced effect on the microstructure of the alloys when compared to the SA heat treatment. First, coarser precipitates were found along the GBs which is shown in Fig. 1a, d, e, and f. The precipitation of secondary phases, such as δ and/or η , was promoted as well. Second, the γ' and/or γ'' precipitates were also coarser following HTA compared to SA, by comparing Fig. 2a-d to Fig. 2e-h. That is, the higher temperature of the HTA heat treatment accelerated the kinetics of phase formation. Furthermore, the first step of the HTA was not only higher than SA (800 °C compared to 730 °C) but also longer (20 h compared to 8 h) which enabled

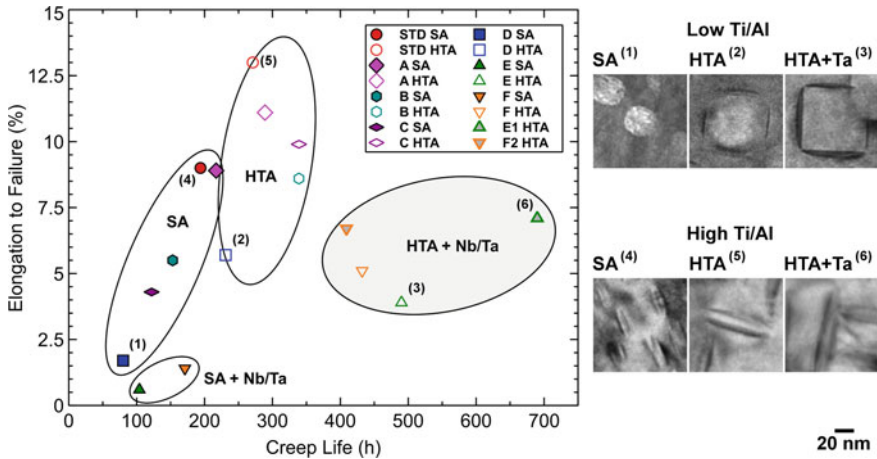


Fig. 7 Elongation to failure as a function of creep life for testing at 700 °C and 483 MPa for the alloys following the SA and HTA heat treatments with TEM images of the γ'/γ'' precipitates taken in the gage section

the coarsening of the various precipitate phases. Note: the solvus temperature of the γ'' phase was predicted from JMatPro to be between 820 °C and 860 °C depending on the alloy formulation, therefore, the first step of the HTA was below the solvus for γ'' and mechanical testing was also performed at temperatures below the γ'' solvus temperature. Secondary precipitation along the GBs has been the subject of numerous studies on IN718, particularly regarding δ phase precipitates. Typically, an additional step is used above the γ'' solvus temperature to promote the formation of δ precipitates [22]. With the highest temperature in the HTA heat treatment being below the γ'' solvus temperature, it is not surprising to see little to no precipitation of δ phase (depending on the variant) in the aged condition while fault-free γ'' precipitates are present in the microstructure. However, these γ'' precipitates are expected to transform (at least partially) to δ phase with fault accumulation during prolonged creep exposure or aging.

The effect of the HTA on the creep performance of the alloys was considerable. An overview is presented in Fig. 7 in which the alloys in the SA condition are compared to those in the HTA condition. Furthermore, the alloys with the Nb/Ta additions are also compared in the SA condition (SA + Nb/Ta) and HTA condition (HTA + Nb/Ta). Significant increases in both creep life and elongation to failure were measured between the SA and HTA heat treatments. Table 2 summarizes the percent increase in creep life and creep ductility when using the HTA instead of the SA heat treatment. The greatest improvements were measured for the alloys with the Nb and Ta additions, particularly alloy E which showed a 371% increase in creep life and 550% increase in creep ductility. Alloy STD SA, most representative of IN725, showed a 40% increase in creep life and 53% increase in creep ductility if the HTA heat treatment is used. With the HTA promoting precipitation strengthening

Table 2 Percent increase in creep life and elongation to failure from the SA to the HTA heat treatment for testing at 700 °C and 483 MPa

Alloy	Ta (at.%)	Nb (at.%)	Ti/Al	% increase in elongation to failure	% increase in creep life
STD	0.04	1.77	4.3	53	40
A	0.10	1.74	5.4	25	33
B	0.10	1.81	1.3	56	122
C	0.11	1.81	1.1	130	178
D	0.10	1.80	0.7	235	189
E	0.95	1.82	0.7	550	371
F	0.10	2.39	0.8	264	153

as well as precipitation at the GBs, additional obstacles to dislocation motion were formed which benefited the creep performance of the alloys. Furthermore, the right-hand side of the figure shows TEM micrographs of the post-creep microstructures. As can be seen, the γ'/γ'' precipitates remained relatively constant and only slight coarsening occurred compared to the aged conditions. Interestingly, alloy D HTA which did not form γ'' precipitates after aging, Fig. 2f, shows thin γ'' precipitates at the γ' cube faces. These likely formed during the lower temperature creep exposure. The precipitate stability in terms of size is deemed beneficial for long-term creep exposures where precipitate coarsening typically leads to deterioration of the creep resistance.

The Role of Nb and Ta Additions

Additions of Nb or Ta were made to high Ti/Al ratio alloy STD to form alloys E1 (Ta-rich variant) and F2 (Nb-rich variant) and to low Ti/Al ratio alloy D to form alloys E (Ta-rich) and F (Nb-rich). The sum of Nb + Ta in alloys E1, F2, E, and F was kept nominally constant at 2.7 at.%. Adding Ta or Nb to STD, Fig. 2e, resulted in a greater density of γ'' precipitates, as shown in alloy E1, Fig. 3a, and F2, Fig. 3b. The addition of Nb was found more beneficial in promoting the formation of γ'' which was expected considering the composition of the γ'' phase, heavily comprised of Nb. In the low Ti/Al ratio alloys, the additions also led to the precipitation of γ'' ; however, since these alloys contained a dense repartition of γ' precipitates, the γ'' phase formed at the γ/γ' interfaces to form compact precipitates, Fig. 4b. It should be noted that the effect of the additions was mostly concentrated within the grains for the high Ti/Al ratio alloys which contained predominantly γ'' precipitates while the effect was more pronounced towards the GBs for the low Ti/Al ratio alloys, as shown in Fig. 1e and f, where δ phase precipitates were present. With more γ' present in the low Ti/Al alloys, the Nb and Ta likely partitioned to the GB phases as opposed to γ'' in the high Ti/Al alloys. Nevertheless, avoiding δ phase formation at the GBs in a γ''

containing alloy may be preferable according to recent findings from Nicolay et al. [23] on IN718. The authors revealed improved mechanical properties by avoiding the first step of the three-step heat treatment, thereby reducing δ formation at the GBs and increasing the amount of γ'' precipitates within the grains, since those phases have similar compositions.

The Nb and Ta additions, as expected considering their impact on the microstructure of the alloys, were associated with significant improvements in the creep life of the alloys particularly when combined with the HTA heat treatment, as shown in Fig. 7. As such, the creep life of those alloys was between 409 and 690 h compared to 194 h for STD (and 271 h in the HTA condition) and 80 h for D (231 h in the HTA condition). The greater amount of precipitate strengthening was responsible for decreases in the minimum creep rate, as described in Ref. [19].

Phase Stability

A phase stability study was performed on the alloys following the HTA heat treatment. Specimens were exposed to 700 °C for times ranging from 500 to 10,000 h. Figure 8 provides an overview of the results after 5,000 h exposure. The GB phases, particularly δ -Ni₃Nb (identified using TEM-EDS, not shown) which appear as bright elongated platelets, coarsened when compared to the as-aged conditions of Fig. 1. Interestingly, alloys STD, E1, F2, and D were found to evolve in a similar manner. Alloy D did not contain as much δ precipitates compared to the other alloys. Alloys E and F, however, revealed extensive formation and growth of the δ phase as well as the formation of intragranular α -Cr precipitates, which appear black in the SEM images of Fig. 8e and f. Such α -Cr precipitate formation has been associated with the formation of intragranular δ -Ni₃Nb in IN718, as the δ phase rejects Cr at longer exposures and results in a local enrichment at the γ/δ interface [24]. Interestingly, in such cases, α -Cr is observed at temperatures <650 °C, while σ phase is observed at higher temperatures [25]. The stability range of the α -Cr precipitates in IN725 remains to be explored further (work underway) as IN718 contains a significantly higher level of Fe which would typically stabilize the σ phase. The lower Ti/Al ratio in alloys E and F predominantly stabilized the γ' as opposed to γ'' . In the high Ti/Al ratio alloys E1 and F2, the γ'' phase ties up elements prone to the formation of δ phase, such as Nb. Therefore, formation of δ phase was retarded in those alloys. Eventually, δ forms as shown in the inset of Fig. 8c after 10,000 h exposure at 700 °C. It is important to note that γ'' is metastable and eventually transforms into its stable δ form [26].

Higher resolution images of the $\gamma/\gamma'/\gamma''$ microstructures of D, E, and F in the HTA condition and after 10,000 h of exposure at 700 °C were taken using TEM and the results are shown in Fig. 9. The $[001]_{\gamma}$ diffraction patterns of each condition show distinct γ'' reflections at differing intensities (D being the weakest, while F shows strong intensity reflections). The shared (100) γ'/γ'' reflections (in red circle) were used for DF imaging and these images show that all three microstructures contain γ' and γ'' precipitates, where the γ'' fraction increases in order of F > E > D. To confirm

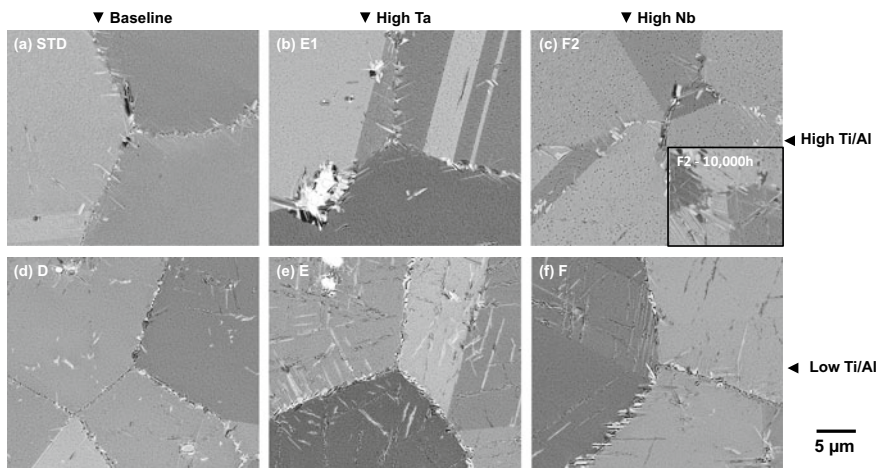


Fig. 8 SEM images of long-term exposure of alloy **a** STD, **b** E1, **c** F2, **d** D, **e** E, and **f** F at 700 °C for 5,000 h following HTA with inset for alloy F2 following 10,000 h exposure

the presence of the γ'' precipitates, intensity line profiles across the shown reflections were measured, and the results are shown in Fig. 9e. Notice that although weak, there is still a γ'' signal for alloy D, whereas this phase was absent after HTA, as shown in Fig. 2f, but present after creep at 700 °C and 483 MPa, Fig. 7. This suggests that the γ'' precipitates form during the 700 °C exposure at certain γ' precipitate faces (and quite often a γ'' precipitate is sandwiched between two γ' precipitates—the formation of this configuration remains to be explored further). As part of the analysis, the mean diameter of at least 40 γ' precipitates after HTA and 10,000 h exposure was manually measured, and the results are shown in Fig. 9d. The analysis shows that statistically, the starting γ' sizes are similar at ~45 nm (E having a slightly smaller average size of ~40 nm) and after 10,000 h at 700 °C, the precipitates coarsen to similar levels of ~60 nm (D coarsening slightly more up to ~68 nm). This represents a 50% increase in size after 10,000 h, which shows that these precipitates do not coarsen substantially (in accordance also to the post-creep microstructures), especially considering that 60 nm is still a very fine precipitate size. The alloys with added Ta (E) and Nb (F) and therefore a stronger compact structure (viz. thicker γ'' precipitates) showed lower γ' coarsening compared to alloy D.

Conclusions

Different alloy variants based on IN725 were designed with varying Ti/Al ratio, a high temperature aging (HTA) heat treatment and additions of Ta or Nb to improve the creep performance of the commercial alloy IN725. Compared to the baseline alloy tested at 700 °C/483 MPa, condition most representative of IN725, the HTA

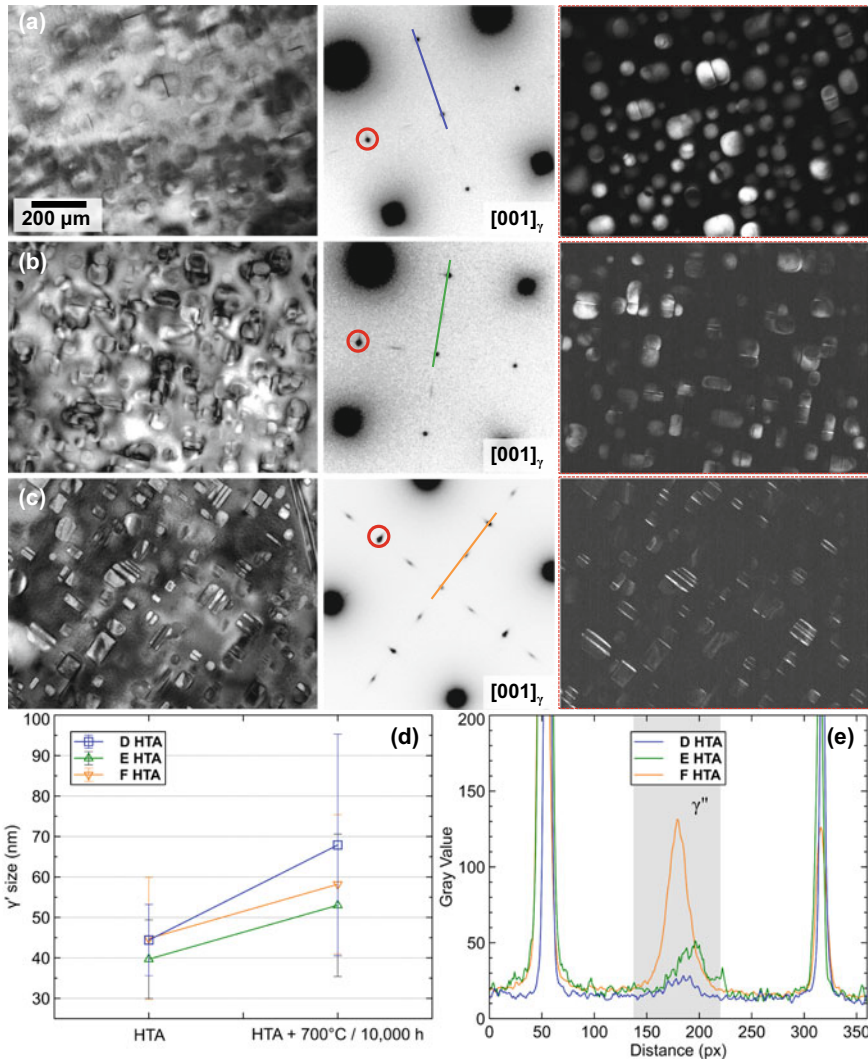


Fig. 9 a–c $\gamma/\gamma'/\gamma''$ microstructures and **d** coarsening behavior of the γ' precipitates in alloys **a** D, **b** E and **c** F following 700 °C exposure for 10,000 h after HTA heat treatment with corresponding TEM BF, SAD and DF images. The DF images were produced with the reflections in red circles in the SAD patterns, while the intensity profiles along the given lines are plotted in **e**

and Nb addition resulted in 111–123% improvement in creep life (depending on the Ti/Al ratio), the HTA and Ta addition resulted in 138–256% improvement in creep life. The following can be concluded:

1. The Ti/Al ratio controlled the stability of γ' vs. γ'' precipitates. While both phases formed in each variant, a high Ti/Al ratio ~ 5 favored formation of predominantly

- γ'' precipitates while a low Ti/Al ~ 1 favored formation of predominantly γ' precipitates. The increase in Al was greater than the decrease in Ti. The creep life and ductility were reduced with decreasing Ti/Al ratio in the SA condition.
2. The HTA promoted coarsening of the γ'/γ'' precipitates as well as the formation and growth of GB phases. The HTA led to significant increases in creep life and ductility from the creation of additional obstacles for dislocation motion during creep.
 3. Compact precipitates were formed in the low Ti/Al ratio alloys consisting of γ' precipitates surrounded by a γ'' shell. The faces of the γ' precipitates were entirely covered (edge-to-edge) with γ'' that was a few to tens of atomic layers thick in some alloys. The thickness of the γ'' increased with the additions of Nb or Ta.
 4. The compact precipitates did not coarsen substantially after 10,000 h exposure at 700 °C, or after creep at 700 °C/483 MPa, and remained below 70 nm in equivalent diameter. The additions of Ta and Nb were associated with slightly reduced γ' coarsening likely due to a stronger compact structure (due to the thicker γ'' precipitates).
 5. The long-term phase stability was impaired by the additions of Ta and Nb with significant growth of δ precipitates, particularly in the low Ti/Al ratio alloys. In the high Ti/Al ratio alloys, the growth of δ from the GBs was slowed down since the Ta and Nb additions mostly contributed to the increase in γ'' density within the grains.

Acknowledgements This work was performed in support of the US Department of Energy's Fossil Energy Crosscutting Technology Research Program. The authors would like to thank E.R. Argetsinger and J.A. Mendenhall for assistance in melting, C.D. Powell for mechanical testing, R.E. Chinn and C. McKaig for chemistry analysis, and M.B. Fortner for metallographic preparation.

Disclaimer This project was funded by the United States Department of Energy, National Energy Technology Laboratory, in part, through a site support contract. Neither the United States Government nor any agency thereof, nor any of their employees, nor the support contractor, nor any of their employees, makes any warranty, express or implied, or assumes any legal liability or responsibility for the accuracy, completeness, or usefulness of any information, apparatus, product, or process disclosed, or represents that its use would not infringe privately owned rights. Reference herein to any specific commercial product, process, or service by trade name, trademark, manufacturer, or otherwise does not necessarily constitute or imply its endorsement, recommendation, or favoring by the United States Government or any agency thereof. The views and opinions of authors expressed herein do not necessarily state or reflect those of the United States Government or any agency thereof.

References

1. L.E. Shoemaker, Alloys 625 and 725: Trends in properties and applications, 6th Int. Symp. Superalloys 718, 625, 706 Deriv. (2005) 409–418. https://doi.org/10.7449/2005/Superalloys_2005_409_418.

2. Special Metals Corporation, INCONEL alloy 725, 2005. SMC-066.
3. S. Mannan, F. Veltry, Time-Temperature-Transformation Diagram of Alloy 725, in: E.A. Loria (Ed.), *Superalloys 718, 625, 706 Var. Deriv.*, TMS (The Minerals, Metals & Materials Society), 2001: pp. 345–356.
4. R. Cozar, A. Pineau, Influence of the Co/Ni Ratio on the γ' and γ'' Precipitation in Fe-Ni-Co-Ta Alloys, *Metall. Trans.* 5 (1974) 2471–2472.
5. R. Cozar, A. Pineau, Morphology of γ' and γ'' precipitates and thermal stability of inconel 718 type alloys, *Metall. Trans.* 4 (1973) 47–59. <https://doi.org/10.1007/BF02649604>.
6. S.K. Mannan, E.L. Hibner, B.C. Puckett, Physical Metallurgy of Alloys 718, 725, 725HS, and 925 for Service in Aggressive Corrosion Environments, *Corrosion*. (2003) 3125.
7. L. Viskari, Y. Cao, M. Norell, G. Sjöberg, K. Stiller, Grain boundary microstructure and fatigue crack growth in Allvac 718Plus superalloy, *Mater. Sci. Eng. A*. 528 (2011) 2570–2580. <https://doi.org/10.1016/j.msea.2010.11.080>.
8. M. Detrois, P.D. Jablonski, J.A. Hawk, The effect of η phase precipitates on the creep behavior of alloy 263 and variants, *Mater. Sci. Eng. A*. 799 (2021) 140337. <https://doi.org/10.1016/j.msea.2020.140337>.
9. A. Agnoli, M. Bernacki, R. Logé, J.M. Franchet, J. Laigo, N. Bozzolo, Understanding and Modeling of Grain Boundary Pinning in Inconel 718, in: E.S. Huron, R.C. Reed, M.C. Hardy, M.J. Mills, R.E. Montero, P.D. Portella, J. Telesman (Eds.), *Superalloys 2012 12th Int. Symp. Superalloys*, TMS (The Minerals, Metals & Materials Society), 2012: pp. 73–82. <https://doi.org/10.1002/9781118516430.ch8>.
10. E.J. Pickering, H. Mathur, A. Bhowmik, O.M.D.M. Messé, J.S. Barnard, M.C. Hardy, R. Krakow, K. Loehnert, H.J. Stone, C.M.F. Rae, Grain-boundary precipitation in Allvac 718Plus, *Acta Mater.* 60 (2012) 2757–2769. <https://doi.org/10.1016/j.actamat.2012.01.042>.
11. S. Antonov, M. Detrois, R.C. Helmink, S. Tin, Precipitate phase stability and compositional dependence on alloying additions in γ - γ' - δ - η Ni-base superalloys, *J. Alloys Compd.* 626 (2015) 76–86. <https://doi.org/10.1016/j.jallcom.2014.11.155>.
12. M.C. Hardy, M. Detrois, E.T. McDevitt, C. Argyrakis, V. Saraf, P.D. Jablonski, J.A. Hawk, R.C. Buckingham, H.S. Kitaguchi, S. Tin, Solving Recent Challenges for Wrought Ni-Base Superalloys, *Metall. Mater. Trans. A*. 51 (2020) 2626–2650. <https://doi.org/10.1007/s11661-020-05773-6>.
13. E.L. Hibner, H.W. Sizek, S.K. Mannan, Elevated temperature tensile and creep rupture properties of Inconel alloy 725, *Superalloys 718, 625, 716 Deriv.* (1997) 491–501.
14. M. Detrois, K.A. Rozman, P.D. Jablonski, J.A. Hawk, Compositional Design and Mechanical Properties of INCONEL® Alloy 725 Variants, in: E. Ott, X. Liu, J. Andersson, Z. Bi, K. Bockenstedt, I. Dempster, J. Groh, K. Heck, P.D. Jablonski, M. Kaplan, D. Nagahama, C. Sudbrack (Eds.), *Proc. 9th Int. Symp. Superalloy 718 Deriv. Energy, Aerospace, Ind. Appl.*, Springer International Publishing, Pittsburgh, PA, 2018: pp. 421–437. https://doi.org/10.1007/978-3-319-89480-5_26.
15. P.D. Jablonski, J.A. Hawk, Homogenizing Advanced Alloys: Thermodynamic and Kinetic Simulations Followed by Experimental Results, *J. Mater. Eng. Perform.* 26 (2017) 4–13. <https://doi.org/10.1007/s11665-016-2451-3>.
16. ASTM International, ASTM E139-11(2018), Standard Test Methods for Conducting Creep, Creep-Rupture, and Stress-Rupture Tests of Metallic Materials, West Conshohocken, PA, 2018. <https://doi.org/10.1520/E0139-11R18>.
17. ASTM International, ASTM E112-13, Standard Test Methods for Determining Average Grain Size, West Conshohocken, PA, 2013. <https://doi.org/10.1520/E0112-13>.
18. Z. Xu, L. Jiang, J. Dong, Z. Li, X. Zhou, The effect of silicon on precipitation and decomposition behaviors of M6C carbide in a Ni–Mo–Cr superalloy, *J. Alloys Compd.* 620 (2015) 197–203. <https://doi.org/10.1016/j.jallcom.2014.09.112>.
19. M. Detrois, S. Antonov, K.A. Rozman, J.A. Hawk, P.D. Jablonski, Improved Creep and Tensile Properties of a Corrosion Resistant Ni-Based Superalloy Using High Temperature Aging and Nb/Ta Additions, *Metall. Mater. Trans. A*. 53 (2022) 2600–2613. <https://doi.org/10.1007/s11661-022-06690-6>.

20. M. Detroids, P.D. Jablonski, J.A. Hawk, NiCrMoNb Age Hardenable Alloy For Creep Resistant High Temperature Applications, And Methods of Making, US20220186343A1, 2022.
21. M. Detroids, P.D. Jablonski, J.A. Hawk, NiCrMoNb age hardenable alloy for creep-resistant high temperature applications, and methods of making, WO2022132928A1, 2022.
22. H.-Y. Bor, C.-N. Wei, H.T. Nguyen, A.-C. Yeh, C.-M. Kuo, Aging effects on the γ' and γ'' precipitates of Inconel 718 Superalloy, in: E.A. Ott, J.R. Groh, A. Banik, I. Dempster, T.P. Gabb, R. Helmink, X. Liu, A. Mitchell, G.P. Sjöberg, A. Wusatowska-Srnek (Eds.), 7th Int. Symp. Superalloy 718 Deriv., TMS (The Minerals, Metals & Materials Society), 2010: pp. 679–688.
23. A. Nicolăy, J. Franchet, N. Bozzolo, J. Cormier, Metallurgical Analysis of Direct Aging Effect on Tensile and Creep Properties in Inconel 718 Forgings, in: Tin S. et al. (Ed.), Superalloys 2020, Springer, Cham, 2020: pp. 559–569.
24. Z. Bi, J. Dong, M. Zhang, L. Zheng, X. Xie, Mechanism of α -Cr precipitation and crystallographic relationships between α -Cr and δ phases in Inconel 718 alloy after long-time thermal exposure, *Int. J. Miner. Metall. Mater.* 17 (2010) 312–317. <https://doi.org/10.1007/s12613-010-0310-z>.
25. J.F. Radavich, Effect of Alpha Chromium on Long Time Behavior of Alloy 718, in: Superalloys 718, 625, 706 Var. Deriv., TMS, 1997: pp. 409–415. https://doi.org/10.7449/1997/Superalloys_1997_409_415.
26. L.M. Suave, J. Cormier, P. Villechaise, A. Soula, Z. Hervier, D. Bertheau, J. Laigo, Microstructural evolutions during thermal aging of alloy 625: Impact of temperature and forming process, *Metall. Mater. Trans. A* 45 (2014) 2963–2982. <https://doi.org/10.1007/s11661-014-2256-7>.